ELSEVIER

Contents lists available at ScienceDirect

Extreme Mechanics Letters

journal homepage: www.elsevier.com/locate/eml





Rapid prediction of grain boundary network evolution in nanomaterials utilizing a generative machine learning approach

Yuheng Wang a,b , Amirreza Kazemi a,b , Taotao Jing c , Zhengming Ding c , Like Li d , Shengfeng Yang a,b,*

- ^a School of Mechanical Engineering, Purdue University in Indianapolis, Indianapolis, IN 46202, USA
- ^b School of Mechanical Engineering, Purdue University, West Lafayette, IN 47907, USA
- ^c Department of Computer Science, Tulane University, New Orleans, LA 70118, USA
- ^d Department of Mechanical and Aerospace Engineering, University of Central Florida, Orlando, FL 32816, USA

ARTICLE INFO

Keywords: Grain boundary network Nanomaterials Machine learning Generative adversarial networks Evolution prediction

ABSTRACT

Predicting the behavior of nanomaterials under various conditions presents a significant challenge due to their complex microstructures. While high-fidelity modeling techniques, such as molecular dynamics (MD) simulations, are effective, they are also computationally demanding. Machine learning (ML) models have opened new avenues for the rapid exploration of design spaces. In this work, we developed a deep learning framework based on a conditional generative adversarial network (cGAN) to predict the evolution of grain boundary (GB) networks in nanocrystalline materials under mechanical loads, incorporating both morphological and atomic details. We conducted MD simulations on nanocrystalline tungsten and used the resulting ground-truth data to train our cGAN model. We assessed the performance of our cGAN model by comparing it to a Convolutional Autoencoder (ConvAE) model and examining the impact of changes in geometric morphology and loading conditions on the model's performance. Our cGAN model demonstrated high accuracy in predicting GB network evolution under a variety of conditions. This developed framework shows potential for predicting various materials' behaviors across a wide range of nanomaterials.

1. Introduction

Understanding and predicting the behaviors of nanomaterials presents a critical challenge for materials research, given their complex microstructures and the associated dynamic evolutions under various conditions. High-fidelity modeling techniques [1,2], such as molecular dynamics (MD) simulations and first-principle density functional theory (DFT) calculations, are effective but also computationally expensive for predicting structure-property relationships in nanomaterials. This high computational cost often limits the exploration of the design space of nanomaterials. Machine learning (ML), due to its ability to predict material properties with significantly less computational cost, is gaining importance in the field of materials research [3–5]. Consequently, ML models, trained on large material datasets to predict structure-property relationships, have provided new pathways for rapid exploration of design spaces for advanced materials [6–8].

ML models have been developed and utilized to predict a multitude of mechanical properties of materials, including grain boundary energy [9,10], and segregation energy [11]. These models can further optimize the design of the structures [12] and composition [13] of materials to meet specific design targets. In addition to predicting individual quantities of interest, more ML models have also been developed to predict full-field quantities of interest, such as stress distribution [14–22] and fracture behavior [23–26]. Various deep learning techniques have been developed for this purpose. For instance, generative adversarial neural networks (GAN) are a type of deep learning network that can generate image data from noise, with properties comparable to training data input. A conditional generative adversarial network (cGAN) [27], a form of GAN, is conditioned with additional information and has been used to predict stress distribution [19,20].

In this study, building on this body of knowledge and recent developments of state-of-the-art cGAN models, we explore their application for predicting the evolution of grain boundary (GB) networks in nanomaterials at the atomic level. As GBs play a crucial role in determining the properties and mechanical behavior of nanomaterials, there is a need to develop an ML model considering both the crystalline

^{*} Corresponding author at: School of Mechanical Engineering, Purdue University in Indianapolis, Indianapolis, IN 46202, USA. *E-mail address:* shengfengyang@purdue.edu (S. Yang).

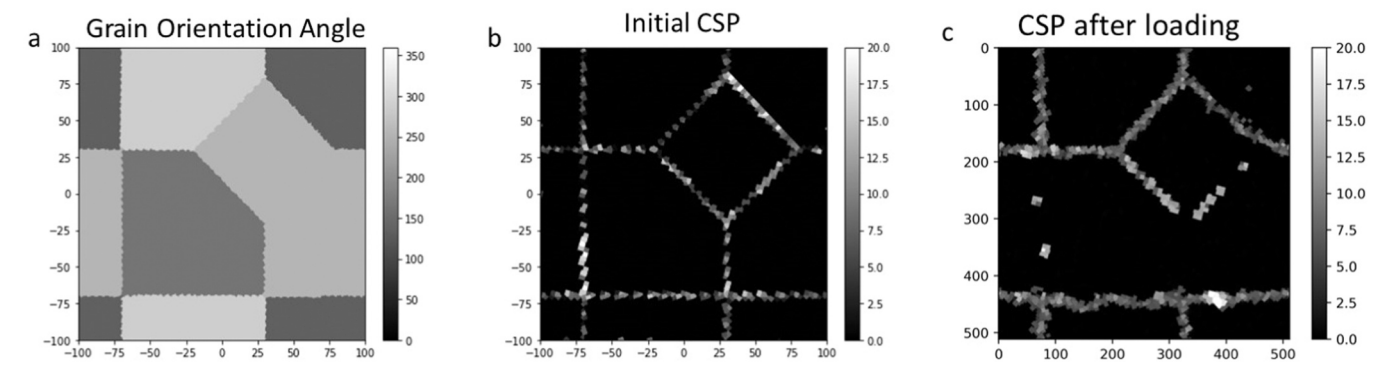


Fig. 1. Evolution of the grain boundary (GB) network in polycrystalline tungsten according to MD simulations: (a) Initial distribution of the orientation angle for each grain within the polycrystalline sample; (b) Initial structure of the GB network, as represented by the Centrosymmetry Parameter (CSP), which indicates the lattice disorder for each atom (with atoms in the bulk region having a CSP close to zero, and atoms in GB regions showing high values); and (c) Deformed GB network structure, represented by the CSP, following a specific loading process that includes relaxation, shearing, and unloading.

morphology and atomic-level details of GBs in predicting the dynamic deformation behaviors of nanomaterials.

As such, our objective in this work is to establish a cGAN-based deep learning framework to predict the evolution of the GB network in nanocrystalline materials under mechanical loadings, incorporating multimodal information – both the morphology of nanocrystalline materials like grain orientation and size distribution, and atomic details at grain boundaries. While this work focuses on the mechanical deformation of nanocrystalline metals, the developed framework can potentially be applied to predict various material behaviors across a wide range of nanomaterials.

2. Methodology

2.1. Molecular dynamics (MD) simulations

MD simulations of nanocrystalline tungsten are performed, yielding atomic-level details in the microstructure evolution of interacting grain boundaries (GBs). The atomic interactions are modeled using an EAM/ FS interatomic potential [28]. The initial atomic models of nanocrystalline Tungsten (W) materials are generated through a random Voronoi tessellation using the open-source package, ATOMSK [29]. The crystal orientation for each grain in the geometric models is randomly chosen, and a total of 1,000 nanocrystalline geometric models with different crystal grain orientations are generated. These models have the same 3D dimensions of 200 Å*200 Å*3.15 Å in three directions, representing a 3D thin film structure, since there are only two layers in the z-direction which meet the minimum requirement for maintaining a body-centered cubic (BCC) crystal structure. The atomic model is divided into 5 grains, as shown in Fig. 1(a), all of which are built along the z-axis (<001>). The grain orientation of each grain, i.e., the angle between the [010] direction and the x-axis, is randomly selected from 288°, 253.44°, 163.8°, 62.28°, 232.2°, and 133.92°. To prevent the grain boundary from overlapping with the edges of the models, all models are shifted 15 Å in the x and y-directions.

The atomic-level microstructure of the GB network in the simulated nanocrystalline tungsten can be visualized using the centrosymmetry parameter (CSP) to distinguish GB regions from bulk regions in materials. CSP is a structural property used to measure the local disorder around an atom and can be calculated using the following equation: $CSP = \sum_{i=1}^4 |\overrightarrow{r_i} + \overrightarrow{r_{i+4}}|^2$. In this equation, 4 is half of the nearest neighbor numbers, which is 8 for BCC crystalline materials. $\overrightarrow{r_i}$ and $\overrightarrow{r_{i+4}}$ are position vectors from the central atom to its neighbor. For an ideal crystal without any defects, $\overrightarrow{r_i}$ and $\overrightarrow{r_{i+4}}$ are in the opposite direction and the same length, so the CSP is 0. However, if defects exist, $\overrightarrow{r_i}$ and $\overrightarrow{r_{i+4}}$ will be different, and thus the CSP is non-zero. Therefore, as shown in Fig. 1(b), the CSP for atoms in the bulk is zero, while it is non-zero for atoms in the

regions of GBs.

Based on the initial atomic structures of the polycrystalline models, their initial CSP contours are calculated. CSP and grain orientation values are calculated for each atom. Subsequently, we compute a Voronoi polyhedron for each atom, ensuring that these polyhedrons do not overlap. When assigning CSP and grain orientation values to pixels, rather than averaging the volume, we identify which Voronoi polyhedron encompasses each pixel. Thus, if a pixel is located within the volume of a specific atom's Voronoi polyhedron, it is assigned the CSP and grain orientation values of that atom. This method allows for a precise and accurate translation of atomic-level data into the pixelated image format used in our visualizations. The atomic structures with corresponding CSP values are converted into images of CSP contours 512*512 pixels, as shown in Fig. 1(b). The contour of the grain orientation angle for each grain is also converted into images with 512*512 pixels. These images will serve as input for the ML model.

MD simulations are performed on the initial models following a specific loading process that includes relaxation, shearing, and unloading. After relaxation is performed, the initial nanocrystalline models are subjected to a cycle of shearing and unloading, i.e., shearing the models by a shear strain of 10% and then fully unloading. Shear loading is applied to both the left and right sides of the specimen. The strain rate applied is $1 \times 10^9 s^{-1}$. For both relaxation and shearing phases, an NPT ensemble with zero pressure is used, and the temperature is maintained at 300 K. The microstructure evolution of these nanocrystalline models during the loading and unloading is modeled with MD simulations using LAMMPS [30]. The CSP contours for the deformed models after the loading process are also calculated and converted into images with 512*512 pixels as shown in Fig. 1(c). As seen from Fig. 1(b), the initial structure of the GB network of a sample is shown by the initial CSP, and GBs between any two neighboring grains are clearly displayed. However, after the loading process including relaxation, shearing, and unloading, the GB network shown in Fig. 1(c) exhibits some changes compared to the initial structure in Fig. 1(b). For example, the GBs between some grains disappear because the differences in the orientation angle between grains are small. Other GBs remain stable after the whole loading process. The evolution of the GB networks heavily depends on the complexity of the microstructure, such as the distribution of grain orientation angles and grain sizes.

2.2. Development of cGAN-based machine learning model

Our objective is to develop an ML model that can efficiently predict the evolution of the microstructure in nanocrystalline materials under certain mechanical loadings. Specifically, we have built a cGAN-based ML model to predict the evolution of the GB network, represented by the contour of the CSP, after a specific loading process. The overall

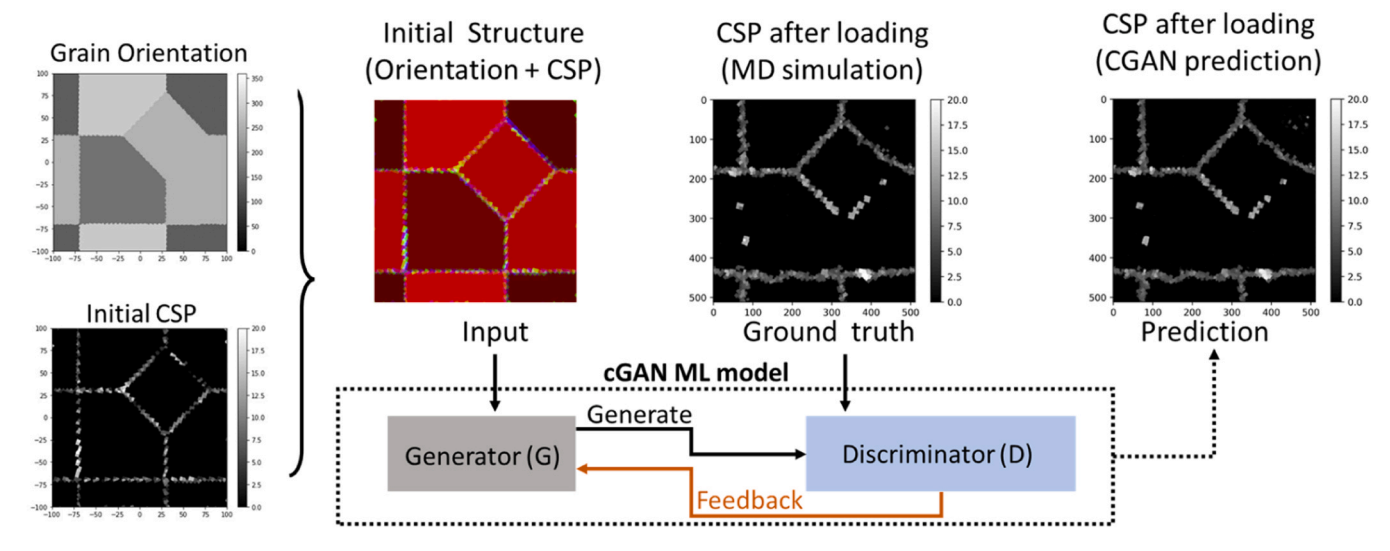


Fig. 2. The workflow of the cGAN-based ML framework for predicting the evolution of grain boundary (GB) networks in polycrystalline materials. The inputs, including initial morphology (grain orientation and size) and atomic information (CSP), are fed to the generator (G) in the cGAN. G generates a prediction of the GB network post-loading, which is sent to the discriminator (D). D compares the prediction with the ground truth and provides feedback to G to enhance the accuracy of GB network evolution predictions.

workflow of the ML framework is shown in Fig. 2. The ground-truth results of the GB network's evolution, represented by the CSP contours, are obtained from MD simulations. These results are converted to images and used as training data for the cGAN model development.

The cGAN is an ML algorithm that is apt for facilitating image-toimage transitions. Similar to the traditional generative adversarial network (GAN) model, the cGAN is divided into two components: a generator (G) and a discriminator (D). In this study, we have developed a cGAN-based model to predict the evolution of the GB network, based on Phillip Isola's work [31]. In our cGAN-based model, the generator is used to generate 'fake' images based on the input of initial crystal orientation and initial CSP contours. The discriminator receives input images from the ground truth (i.e., MD simulation results) or from the G's output and then estimates whether the input is from the ground truth or an output image generated by G. Consequently, the generator and discriminator operate in adversarial roles: the generator tries to 'cheat' the discriminator, while the discriminator tries to maximize the identification rate of fake images. In our cGAN-based ML model, a general shape of a U-Net is used for the generator, and a convolutional PATCH GAN classifier is used for the discriminator. The generator consists of 19 layers, while the discriminator includes 7 layers. Detailed architecture of the generator and the discriminator used in our cGAN model, including the configuration of layers, can be found in Appendix A. The optimizer used for both G and D is Adam. The initial learning rate is set at 0.002. A scheduler is configured to decrease the learning rate from its initial value to zero over 500 epochs. The learning rate decreases linearly every 50 epochs.

3. Results and discussion

3.1. Training the cGAN-based model for predicting GB network evolution

In this work, we trained the cGAN model using two types of inputs: (1) the geometric morphology of materials, which includes information on grain orientations, size, and shape; and (2) the CSP contours of the initial atomistic structures. The outputs are the deformed structures of GB networks, represented by the CSP contours of the models after applying the loading scheme. All these inputs and outputs are converted into images with 512*512 pixels.

We specifically designed the loss function to adapt the conventional cGAN model to predict the GB network evolution for nanocrystalline

materials under mechanical loadings. Unlike the original cGAN model, we formulated the loss function for the generator (G) by combining three different terms: Loss_GAN, Mean Absolute Error (MAE), and Structural Similarity Index Measure (SSIM), as shown in Eq. (1).

$$Loss_{generator} = Loss_{GAN} + \lambda_1 * MAE - \lambda_2 * SSIM$$
 (1)

The GAN loss is a cross-entropy loss, calculated by the predicted image tensor and the ground-truth tensor. In our cGAN model, the GAN loss is a modified form of the conventional GAN loss and can be expressed using Eq. (2). Here, x is the input, y is the output, z is the random noise, and D(x, G(x, z)) is the output of the discriminator.

$$Loss_{GAN} = E_{x,y}[logD(x, G(x, z))]$$
(2)

The MAE loss is calculated by comparing the ground truth and the prediction (Eq. (3)).

$$MAE = \sum_{i,j=1}^{512} |x_{pre}(i,j) - x_{real}(i,j)|$$
 (3)

In addition, we incorporated the SSIM loss into the loss function for the generator. SSIM is widely used to measure the similarity between two images based on three different aspects: luminance, contrast, and structure. SSIM ranges from 0 to 1, where a value close to 1 indicates that two images are similar, while a value close to 0 means that the two images are different. The detailed formulation for SSIM can be found in Appendix B. λ_1 and λ_2 in Eq. (1) are the weights for the MAE and SSIM losses, respectively.

The loss function for the discriminator (D) is the sum of these two components. This loss, shown in Eq. (4), can be divided into two parts, $Loss_{real}$ and $Loss_{fake}$, which are binary cross-entropy losses, as expressed in Eqs. (5) and (6). Unlike the loss for G, for D, the ground-truth image should have a higher score (close to 1), and the fake part should have a lower score (close to 0). Therefore, the real part (Eq. (5)) only has the first term, and the fake loss (Eq. (6)) only has the second term.

$$Loss_{discriminator} = Loss_{real} + Loss_{fake}$$
 (4)

$$Loss_{real} = E_{x,y}[logD(x,y)]$$
 (5)

$$Loss_{fake} = E_{x,z}[log(1 - D(x, G(x, z)))]$$
(6)

We used 80% of the data to train the model, 10% for validation, and 10% for testing the ML model. To quantify how well our cGAN-based ML

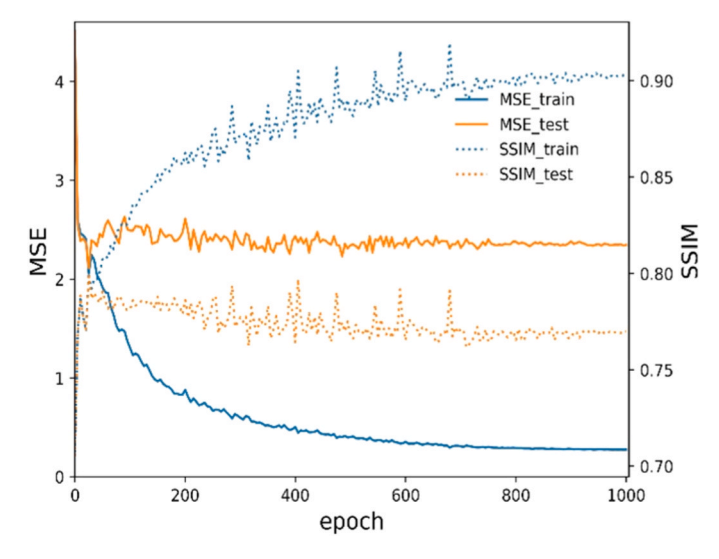


Fig. 3. Converge of evaluation metrics (MSE and SSIM) during the training of the cGAN model.

model fits a dataset during the training stage, we used the metrics of Mean Squared Error (MSE) and SSIM. As shown in Fig. 3, the MSE of the training set decreased to less than 0.5, and the SSIM increased with the number of epochs, reaching 0.90 at the 1,000th epoch. For the test set, the SSIM converged to around 0.77, and the MSE converged to about 2.3. Between 800 and 1,000 epochs, the MSE and SSIM showed stable values, suggesting that the cGAN model converged after 1,000 epochs of training. Therefore, in this study, we trained all models for at least 1,000 epochs to ensure that the training of the cGAN model converged.

3.2. Evaluation of the cGAN-based Model for Predicting GB Network Evolution

In this section, we evaluate the performance of our cGAN model in terms of its accuracy in predicting the evolution of the GB network. Besides comparing it to the ground truth derived from MD simulations, we also contrast our cGAN-based model with another benchmark model, specifically, the Convolutional Autoencoder (ConvAE).

For this purpose, we trained a ConvAE model [32], which has a channel autoencoder structure utilizing residual blocks. Given its capacity for image reconstruction, it can be trained to generate images of the deformed GB network post-loading.

We conducted a comparison of the GB network predictions between the cGAN and ConvAE models, and the ground truth from MD simulations. Fig. 4 presents a side-by-side comparison of images from the cGAN model, the ground truth, and the ConvAE model. Evidently, the cGAN model provides a more accurate prediction of the GB network structure. The cGAN model outperforms the ConvAE model in predicting the evolution of the GB structure, and the luminance of the cGAN prediction closely aligns with that of the ground truth, whereas the ConvAE prediction is considerably darker.

To quantitatively evaluate the accuracy of our cGAN model in predicting the evolution of the GB network, we employed three distinct types of metrics. First, in Section 3.2.1, we utilized global metrics such as MAE, MSE, and SSIM for an image-to-image comparison between the ground truth and the predictions. Second, we developed binary classification accuracy metrics to assess our model's performance in differentiating GB regions from the bulk regions, as discussed in Section 3.2.2.

 Table 1

 Comparative analysis of predictions from cGAN and ConvAE models.

	cGAN	ConvAE
MAE	0.4161	0.4820
MSE	2.3445	1.9702
SSIM	0.7699	0.6934

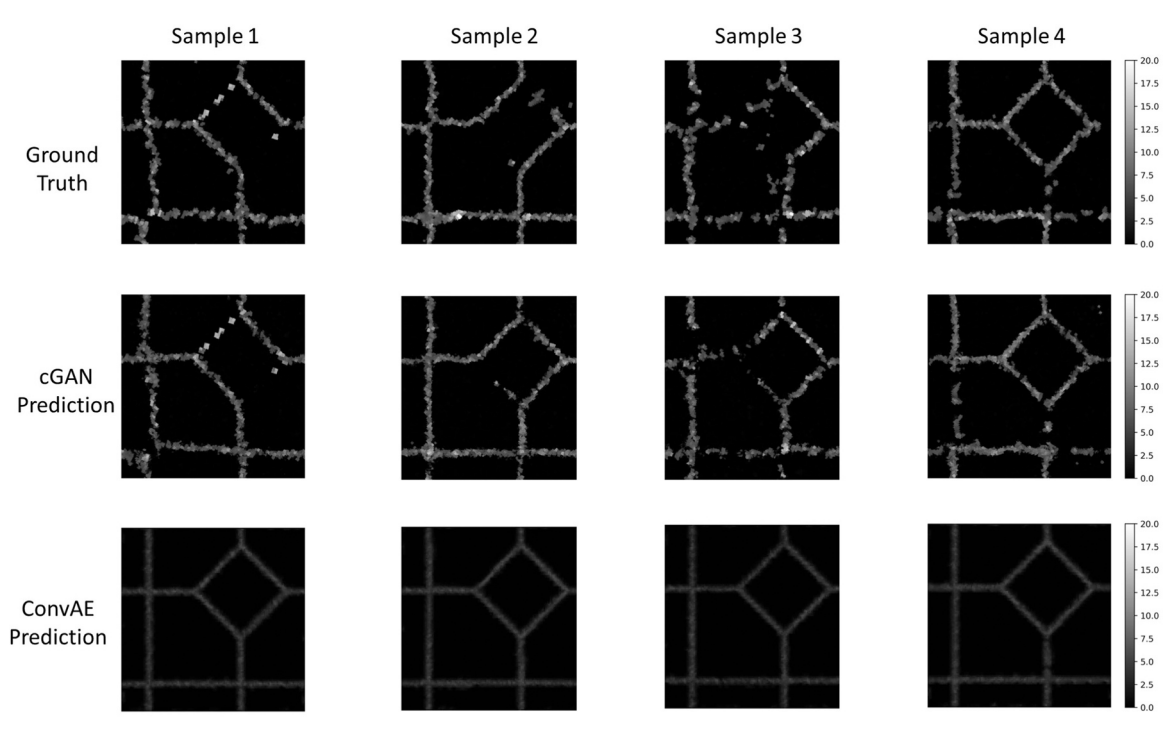


Fig. 4. Comparison of predictions of GB network represented by CSP contours from the cGAN and ConvAE models with the ground truth for four different samples. Each column represents results for a specific sample. The first row displays the ground truth from MD simulation results after loading, the second row shows the prediction from the trained cGAN model, and the last row illustrates the prediction from the trained ConvAE model.

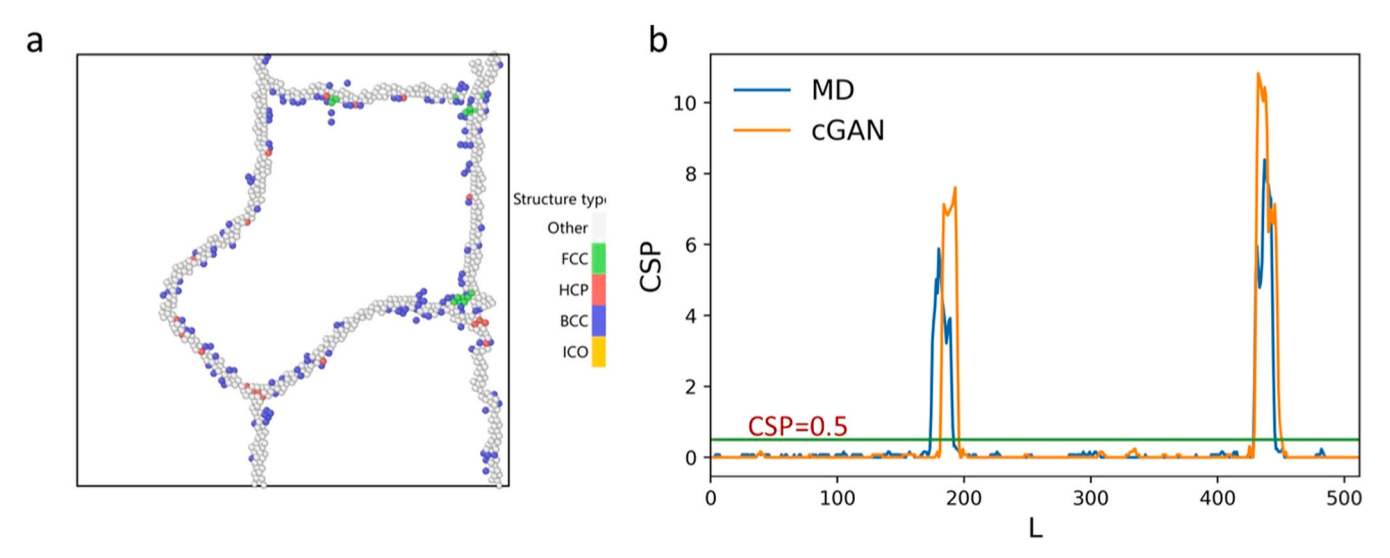


Fig. 5. (a) GB network colored by crystal phases. Only atoms with a CSP larger than 0.5 are displayed; (b) Comparison between the ground truth and predicted CSP distribution along a crossline to identify the location of GBs. The solid straight line indicates the CSP = 0.5 threshold for distinguishing GB and bulk regions.

Finally, in Section 3.2.3, we introduced a novel type of metric to evaluate our cGAN model's performance in predicting the distribution of GB regions.

3.2.1. Quantitative image-to-image evaluation using global metrics

In Table 1, we present a quantitative image-to-image comparison between the ground truth and the predicted outcomes, employing three global metrics: MAE, MSE, and SSIM. The SSIM values for the cGAN and ConvAE models are 0.7699 and 0.6934, respectively, indicating that our cGAN model performs significantly better as a higher SSIM value corresponds to superior prediction quality. Moreover, our cGAN model surpasses the ConvAE model in reducing MAE. However, the ConvAE model outperforms the cGAN model in terms of MSE.

This suggests that while the ConvAE model has focused more on minimizing MSE, it falls behind in MAE and SSIM compared to the cGAN model. Considering that our study's objective is to predict the evolution of the GB network - which occupies a much smaller area than the bulk regions - the SSIM seems to be a more accurate evaluation metric than the MSE for our specific context of GB network evolution, as further confirmed by the comparison in Fig. 4 and the quantitative comparison in Table 1.

However, these metrics, including MAE, MSE, and SSIM, treat all pixels in the images equally and are therefore unable to differentiate the GB regions from the bulk regions. Since our study aims to improve prediction accuracy specifically for the GB network, it is crucial to introduce more precise evaluation metrics for assessing a model's performance in predicting the GB network. We will address this issue in the next two sections.

3.2.2. Quantitative evaluation using binary classification metrics

In the previous section, we analyzed global metrics (MAE, MSE, and SSIM) which do not differentiate between the GB and bulk regions. However, given that the GB regions hold more importance in our study, it's crucial to develop evaluation metrics that pay special attention to these areas.

This section, therefore, introduces a method of distinguishing each pixel in the predicted image as belonging either to the GB or the bulk region. Our problem thus transforms into a binary classification task for each pixel in the image, labeling it as a bulk or a GB pixel. The model's evaluation criterion now lies in its ability to correctly classify each pixel.

Pixels exceeding a particular threshold in the CSP value are classified as grain boundary (GB) pixels. This threshold was meticulously determined to ensure all atoms within GB regions have a CSP value exceeding

it, while atoms within the bulk have lower values. In Fig. 5(b), the horizontal line, which indicates a CSP threshold of 0.5, predominantly encompasses GB pixels and effectively eliminates all bulk pixels. Utilizing the Open Visualization Tool (OVITO), we distinctly delineate the GB network, wherein all atoms possessing a CSP value exceeding 0.5 are identified as GB atoms, as shown in Fig. 5(a). This graphical representation efficiently highlights all existing GBs, as evidenced in Fig. 5(a), while concurrently preventing the erroneous inclusion of any atoms within the bulk region into the GB network.

For a quantitative assessment of our ML model's ability to predict GB regions in the deformed structure of nanocrystalline materials, we employ Pratt's Figure of Merit (PFoM) [33,34] to measure the GB region prediction accuracy. This metric compares the ground truth and the predicted image in terms of binary classification of GB and bulk regions. The PFoM is defined by the following equation:

$$PFoM = \frac{1}{\max(N_{real_{GB}}, N_{fake_{GB}})} \sum_{i=1}^{N_{fake_{GB}}} \frac{1}{1 + \xi d_i^2} . \tag{7}$$

In the equation, $N_{real_{GB}}$ and $N_{fake_{GB}}$ denote the number of GB pixels whose CSP value is smaller than the threshold in the ground truth and predicted images, respectively, ξ is a constant used to scale the value within a suitable range [35], and in this study, it is set to 0.1, and d_i represents the L₂-norm distance from the i-th GB pixel to the nearest GB pixel in the images.

Additionally, in our study, we modified and utilized the commonly used metrics of recall and precision, which are commonly used in binary classification problems. Recall is defined as the ratio of correctly predicted GB pixels to the total number of GB pixels in the ground truth:

$$Recall = \frac{1}{N_{real_{GB}}} \sum_{i=1}^{N_{real_{GB}}} \max(sign(D^2 - g_i^2), \quad 0).$$
 (8)

Precision is defined as the ratio of correctly predicted GB pixels to the total number of predicted GB pixels:

$$\text{Precision} = \frac{1}{N_{fake_{GB}}} \sum_{i=1}^{N_{fake_{GB}}} \max(sign(D^2 - d_i^2), \quad 0). \tag{9}$$

Here, D represents a constant standard distance used to determine whether a pixel is predicted correctly or incorrectly, and in our study, we set D to B. If the distance B is smaller than B, the prediction is considered correct; otherwise, it is considered incorrect. The term B represents the B-norm distance of the B-th B-pixel in the ground truth

Table 2Comparative analysis of predictions for distinguishing GB regions.

	cGAN	ConvAE
PFoM	0.8314	0.6683
Recall	0.9406	0.9485
Precision	0.9470	0.7954

to the nearest GB pixel in the predicted images. The CSP threshold of 0.5 is used to distinguish between GB and bulk regions.

The results, shown in Table 2, reveal that compared to the ConvAE baseline model, the cGAN model exhibits superior performance in terms of PFoM and Precision, although it lags slightly in Recall. Overall, the cGAN model performs better than the ConvAE model at distinguishing GB regions from bulk regions.

3.2.3. Quantitative evaluation using GB neighbor ratio

The evaluation metrics detailed in the previous section are primarily concerned with differentiating whether a pixel belongs to the GB or the bulk region. This section takes a further step by focusing on the accuracy of predicting the neighboring environment for each pixel. To this end, we introduce the concept of the GB neighbor ratio.

We continue to use a threshold of 0.5 for the CSP value to distinguish between GB pixels and bulk pixels. The GB neighbor ratio is then defined as the ratio of GB pixels to all neighboring pixels. A GB neighbor ratio of 0 indicates that all neighboring pixels are bulk pixels, while a ratio of 1 signifies that all neighboring pixels are GB pixels.

We demonstrate a comparison of the CSP value distribution between our cGAN model and the ground truth in Fig. 6(a-d). The comparison shows that our cGAN model has a strong capacity for accurately predicting GB locations. Further examination of the GB neighbor ratio distribution in Fig. 6(e) reveals that the predicted images contain slightly more GB pixels than the ground truth, as evidenced by the marginally higher values.

To provide a more comprehensive view, we calculate the average GB neighbor ratio for a predicted image of the GB network. This is achieved using the following formula: $AVG(R_{GB_neighbor}) = \frac{1}{L_vL_v} \sum_{i,j=1}^{L_xL_y} R_{GB_neighbor}(i,j)$.

In this equation, $R_{GB,neighbor}$ represents the GB neighbor ratio for each pixel in the image, and L_x and L_y correspond to the lengths of the sample in pixels.

In Fig. 6(f), we compare the average GB neighbor ratios predicted by both the ConvAE and cGAN models across 30 test samples. The comparison reveals that the cGAN model performs better, especially in the lower range of the distribution, closely aligning with ground truth values.

In summary, the comparisons across various evaluation metrics clearly underscore the superior predictive capability of the cGAN model in forecasting the evolution of the GB network.

3.3. Investigation into factors affecting the performance of the cGAN model

In this section, we delve into the investigation of various factors that could potentially influence the performance of the cGAN Model. Specifically, we explore the implications of input features representing the GB network, the geometric morphology of crystal grains, and the different loading conditions.

3.3.1. Effects of additional input features for representing the GB network In Section 3.2, we relied solely on the CSP to differentiate atoms within GB regions from those in bulk regions. In this section, we investigate whether this single feature is sufficient, or whether additional features could improve our model's accuracy. Specifically, we consider the excess free volume (V_{Free}) and the bond orientational order (Q_{10}) for each atom.

The V_{Free} represents the additional volume an atom occupies compared to a regular lattice bulk environment. This feature can potentially distinguish between atoms in GB regions and those in bulk regions due to differences in their excess free volumes. On the other hand, the Q_{10} quantifies the spatial distribution of neighboring atoms. It represents the spherical harmonic between a central atom and its neighbors, as defined by the following equations:

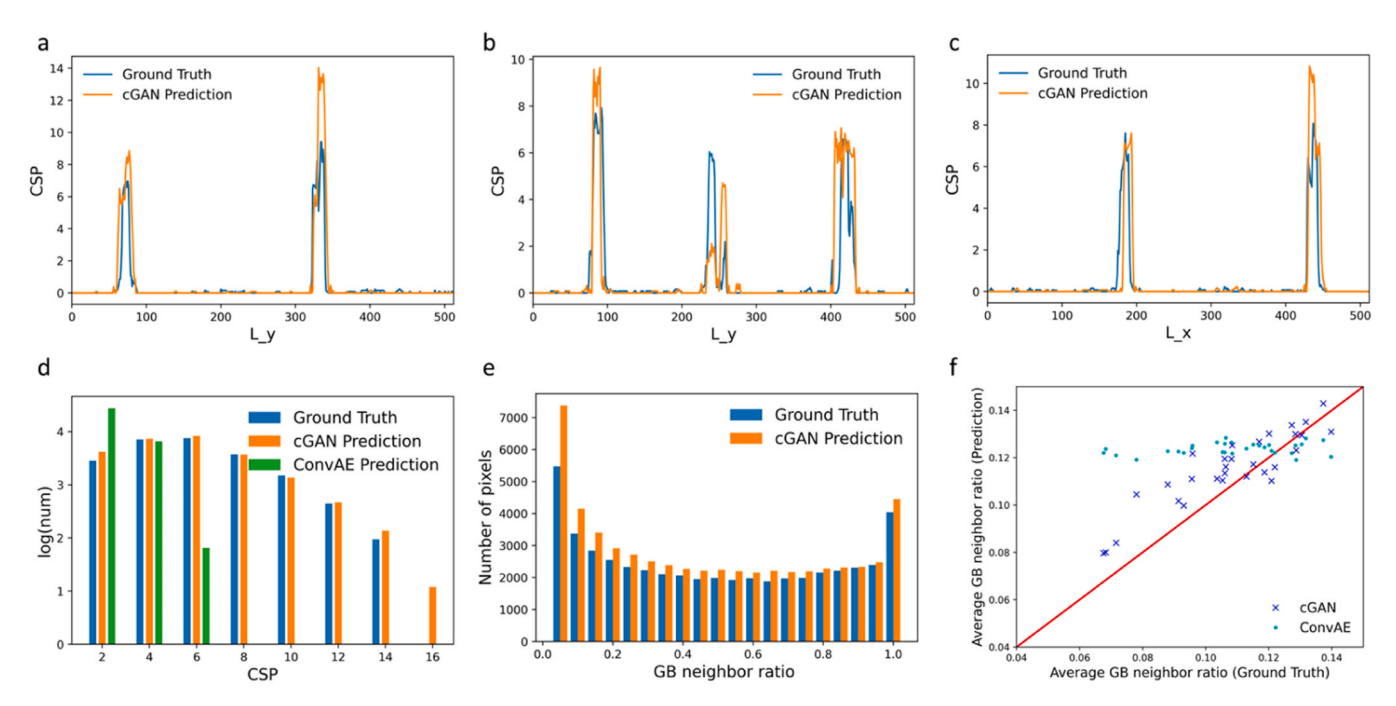


Fig. 6. Quantitative evaluation of the cGAN model by comparing to ground truth and ConvAE predictions: the CSP along the y-direction at different locations of (a) x = 20 Å and (b) x = 220 Å, (c) the CSP of a slide along the x-direction; (d) the CSP distribution; (e) the distribution of GB neighbor ratio for the ground truth and predicted images; (f) the average GB neighbor ratio from predictions versus ground truth for both cGAN and ConvAE models.

Table 3Comparison of PFoM, Recall, and Precision for different input features.

Extra Input Feature	PFoM	Recall	Precision
None (CSP only)	0.8314	0.9406	0.9470
Q_{10}	0.8159	0.9496	0.9151
V_{Free}	0.8152	0.9499	0.9144
Q_{10}, V_{Free}	0.8185	0.9507	0.9165

$$q_m(i) = \frac{1}{N_b} \sum_{j=1}^{N_b} Y_m(\theta(\overrightarrow{r_{ij}}), \varphi(\overrightarrow{r_{ij}}))$$
(10)

$$Q_{10}(i) = \sqrt{\frac{4\pi}{21} \sum_{m=-10}^{10} |q_m(i)|^2}$$
 (11)

where i is the index of the central atom, j refers to a neighboring atom, and N_b represents the number of neighboring atoms.

We expanded our model inputs to include bond orientational order and excess free volume, alongside CSP, to describe the GB network. We tested these features both individually and in combination. Table 3 provides a comparison of results for different combinations of input features. Interestingly, the model using only CSP (i.e., without any additional features) slightly outperforms other cases in terms of PFoM, scoring 0.8314 compared to the range of 0.81–0.82 for models with additional features. This result supports the use of CSP alone as it yields

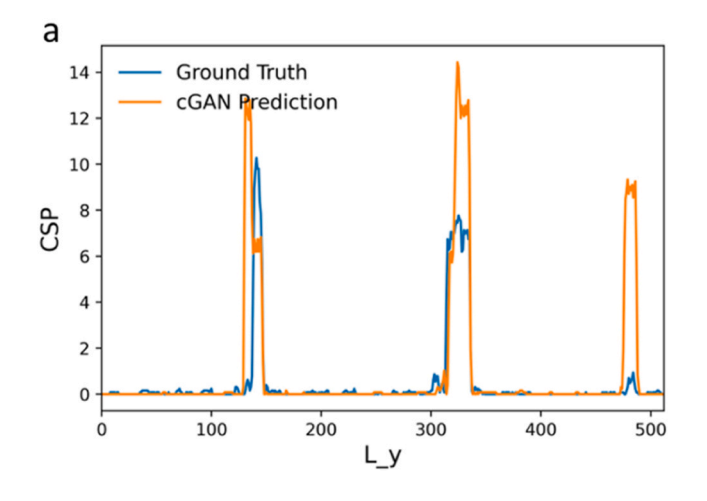
a higher PFoM.

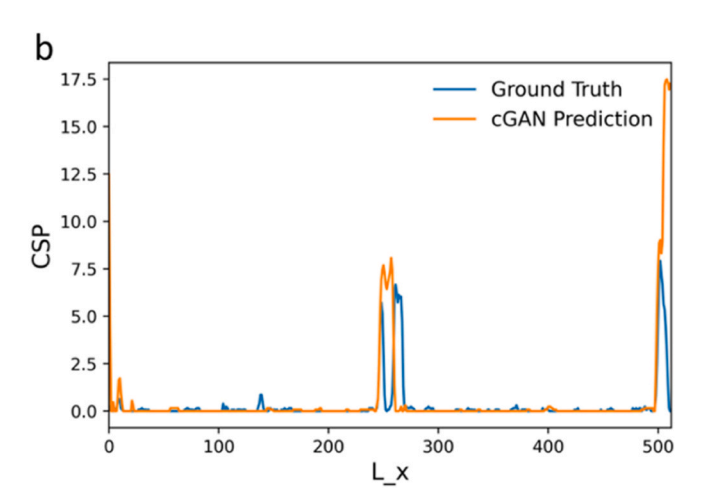
Further examination of Recall and Precision reveals that the model without additional features presents slightly lower Recall but higher Precision than other cases. This indicates that the introduction of V_{Free} and Q_{10} doesn't significantly improve prediction, largely due to their overlapping influences with the basic CSP input feature. Thus, this additional analysis suggests that the CSP feature alone is sufficient for differentiating atoms in GBs from those in bulk regions in our cGAN model.

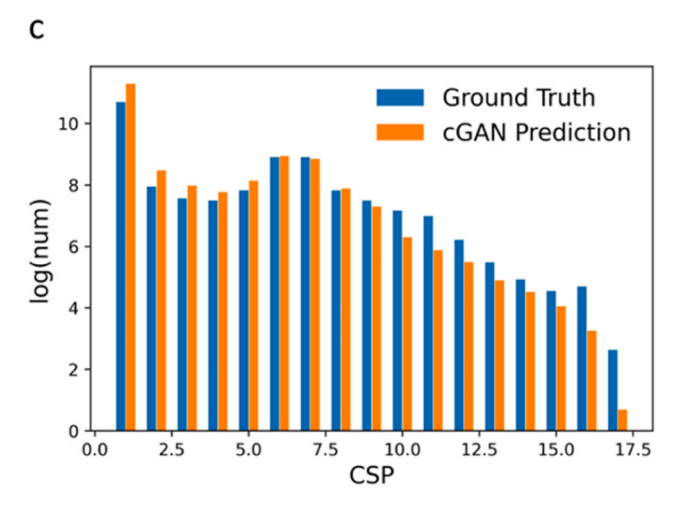
3.3.2. Effects of loading conditions

In the preceding sections, we considered samples subjected to a specific loading process comprising shearing and unloading. This section explores the generalizability of our cGAN model under a different loading condition. Specifically, we apply a shearing strain of 10% to the samples, akin to what we used in previous sections. However, unlike earlier tests, we do not unload the samples, resulting in a final deformed shape that differs from the input images. Therefore, additional adjustments are necessary and were performed for our cGAN model to accommodate these differing shapes between input and output images.

After training our models with the new loading condition, we evaluated the distribution of the CSP and GB neighbor ratio, as shown in Fig. 7. Fig. 7(a) and (b) demonstrate that the cGAN model can still accurately predict the location of GBs in the network following the application of the new loading condition. Compared to the results shown in Fig. 6(d), we observed an increase in the number of pixels with high







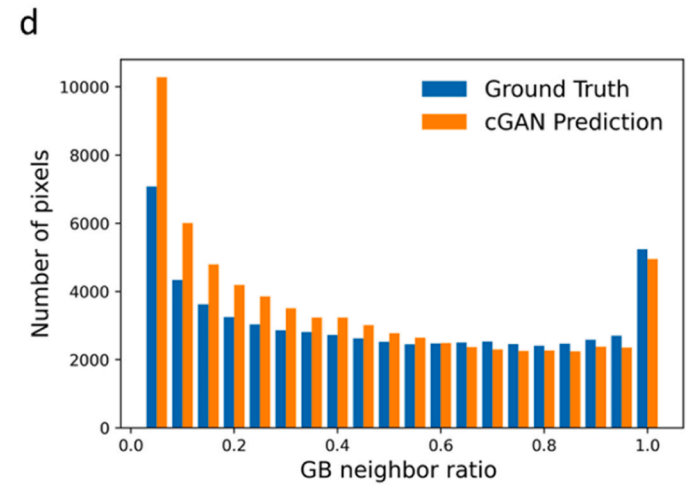


Fig. 7. Quantitative evaluation of the cGAN model by comparing to ground truth: the CSP along the crossline at different locations of (a) x = 220 Å and (b) y = 120 Å, (c) the CSP distribution; and (d) the distribution of GB neighbor ratio in the ground truth and predicted images.

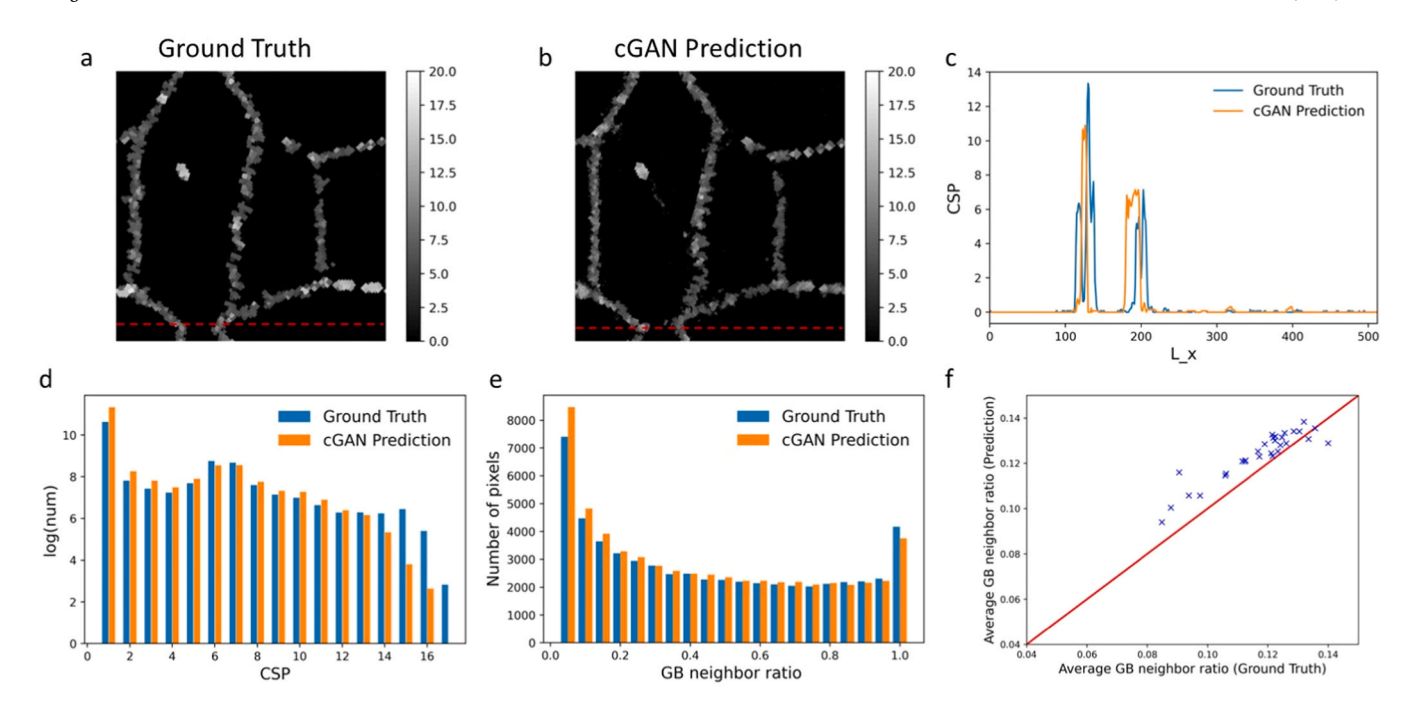


Fig. 8. (a) and (b) show the respective ground truth and predicted image for Geometry B; (c) presents the CSP of a slide along the x-direction; (d) displays the CSP distribution; (e) depicts the distribution of GB neighbor ratio in the ground truth and predicted images; and (f) illustrates the average GB neighbor ratio from the cGAN model and the ground truth.

Table 4Comparison of results for two different types of geometries.

Geometry	MAE	MSE	SSIM	PFoM	Recall	Precision
A	0.4161	2.3445	0.7699	0.8124	0.9456	0.9130
В	0.4128	2.2802	0.7713	0.8492	0.9588	0.9369

CSP values in the samples subjected to the new loading condition, as shown in Fig. 7(c). This increase is likely due to the presence of more defects, such as dislocations and stacking faults, in the bulk region caused by not unloading the samples.

The comparison of the cGAN model predictions to ground truth results (Figs. 7(c) and 7(d)) suggests that the cGAN model continues to perform well in predicting the distribution of the CSP and GB neighbor ratio. Overall, this exploration of a new loading condition demonstrates that our cGAN model retains its predictive power in simulating the evolution of the GB network for nanocrystalline samples under various loading conditions.

3.3.3. Effects of geometric morphology of crystal grains

In all previous sections, our cGAN model was trained and tested on a specific geometric morphology (Geometry A) of the nanocrystalline materials. This geometry featured grains with regular shapes as shown in Fig. 1. In this section, we explore the impact of changes in geometric morphology on the performance of our machine learning model.

We create another geometry, referred to as Geometry B, which also contains five grains. However, unlike Geometry A, the shape and size of the grains in Geometry B are randomly generated, as shown in Fig. 8(a). We apply the same specific loading process to these samples, simulating the evolution of the GB network.

The cGAN model is trained with the same arguments and process as in previous sections. When compared with the results from Geometry A, the cGAN model shows the same or even better accuracy for Geometry B. Table 4 presents the comparison. The MAE and MSE for the Geometry B samples in the test set are 0.4128 and 2.2802, respectively, slightly better than the 0.4161 and 2.3445 for Geometry A samples. The SSIM is 0.7713 for Geometry B, similar to the 0.7699 for Geometry A. Moreover,

the PFoM for Geometry B is 0.8492, an improvement compared to 0.8124 in Geometry A.

Despite the randomly generated grain size and shape in Geometry B, which results in a more complex structure, the model provides slightly better predictions. This could be attributed to the richer details provided by Geometry B, offering more information for the model to learn from. As seen in Figs. 8(a) and 8(b), the predicted image accurately indicates whether the GB will disappear or not, similar to what we observed in Geometry A. Fig. 8(c) shows the CSP of a slice cut along the dashed line in Figs. 8(a) and 8(b), and it illustrates that the cGAN model's prediction of GB locations generally aligns with the ground truth, with minor differences in GB width and maximum CSP values. Figs. 8(d) and 8(e) display the same trend in the distributions of CSP and GB neighbor ratio between predictions and the ground truth for Geometry B.

In conclusion, despite the complexity introduced by changes in geometry, the comparison results demonstrate that such changes do not negatively affect the predictive capability of our cGAN model. This suggests that our cGAN model can be generalized to predict the evolution of the GB network with varying geometrical morphologies.

4. Conclusions

In conclusion, this work presents a novel, cGAN-based machine learning framework for predicting the evolution of the GB network in nanocrystalline materials subjected to mechanical loading conditions. We adapted and trained the cGAN model using MD simulation results, providing a robust and accurate tool for analyzing nanocrystalline materials.

We benchmarked the performance of the cGAN model against a baseline model (ConvAE), showing superior results. To quantitatively evaluate the accuracy of the cGAN model, we introduced three novel types of metrics, including binary classification metrics, to differentiate GBs from the bulk regions.

This study also explores the influence of various factors on the performance of our cGAN model. Specifically, we have shown that the cGAN model is capable of predicting the evolution of GB networks across different geometric morphologies of crystal grains and under various loading conditions, demonstrating its versatility and wide applicability. This work primarily focuses on developing a deep learning model to predict the complex behavior of grain boundary evolution under mechanical loading at room temperature. Given that temperature significantly influences the evolution of grain boundaries, we will consider high-temperature effects, including annealing processes, in our future work.

This research not only provides a powerful tool for predicting GB network evolution, but it also highlights the potential of using machine learning in advancing our understanding of nanocrystalline materials. We expect that this cGAN-based ML framework will pave the way for more precise predictions in material science, ultimately enabling the design and creation of more robust, adaptable materials.

CRediT authorship contribution statement

Yuheng Wang: Writing – review & editing, Writing – original draft, Visualization, Validation, Software, Methodology, Investigation, Formal analysis, Data curation. Amirreza Kazemi: Writing – review & editing, Investigation. Taotao Jing: Writing – review & editing, Methodology. Zhengming Ding: Writing – review & editing, Writing – original draft, Supervision. Like Li: Writing – review & editing, Writing – original draft, Visualization. Shengfeng Yang: Writing – review & editing, Writing – original draft, Supervision, Software, Project administration, Methodology, Formal analysis, Conceptualization.

Declaration of Competing Interest

The authors declare that they have no known competing financial interests or personal relationships that could have appeared to influence the work reported in this paper.

Data Availability

Data will be made available on request.

Acknowledgement

This work is supported by the National Science Foundation under Award Number CMMI-2347035.

Appendix A. Supporting information

Supplementary data associated with this article can be found in the online version at doi:10.1016/j.eml.2024.102172.

References

- [1] E. van der Giessen, P.A. Schultz, N. Bertin, V.V. Bulatov, W. Cai, G. Csányi, S. M. Foiles, M.G.D. Geers, C. González, M. Hütter, W.K. Kim, D.M. Kochmann, J. Llorca, A.E. Mattsson, J. Rottler, A. Shluger, R.B. Sills, I. Steinbach, A. Strachan, E.B. Tadmor, Roadmap on multiscale materials modeling, Model. Simul. Mater. Sci. Eng. 28 (4) (2020) 043001.
- [2] P. Makkar, N.N. Ghosh, A review on the use of DFT for the prediction of the properties of nanomaterials, RSC Adv. 11 (45) (2021) 27897–27924.
- [3] K.T. Butler, F. Oviedo, P. Canepa, Machine Learning in Materials Science, American Chemical Society2022.
- [4] J. Damewood, J. Karaguesian, J.R. Lunger, A.R. Tan, M. Xie, J. Peng, R. Gómez-Bombarelli, Representations of materials for machine learning, Annu Rev. Mater. Res 53 (2023).
- [5] F. Oviedo, J.L. Ferres, T. Buonassisi, K.T. Butler, Interpretable and explainable machine learning for materials science and chemistry, Acc. Mater. Res. 3 (6) (2022) 597–607
- [6] M. Parsazadeh, S. Sharma, N. Dahotre, Towards the next generation of machine learning models in additive manufacturing: a review of process dependent material evolution, Prog. Mater. Sci. 135 (2023) 101102.

- [7] K. Choudhary, B. DeCost, C. Chen, A. Jain, F. Tavazza, R. Cohn, C.W. Park, A. Choudhary, A. Agrawal, S.J. Billinge, Recent advances and applications of deep learning methods in materials science, Npj Comput. Mater. 8 (1) (2022) 59.
- [8] D. Morgan, G. Pilania, A. Couet, B.P. Uberuaga, C. Sun, J. Li, Machine learning in nuclear materials research, Curr. Opin. Solid State Mater. Sci. 26 (2) (2022) 100975
- [9] M. Guziewski, D. Montes de Oca Zapiain, R. Dingreville, S.P. Coleman, Microscopic and macroscopic characterization of grain boundary energy and strength in silicon carbide via machine-learning techniques, ACS Appl. Mater. Interfaces 13 (2) (2021) 3311–3324.
- [10] Y. Wang, X. Li, X. Li, Y. Zhang, Y. Zhang, Y. Xu, Y. Lei, C.S. Liu, X. Wu, Prediction of vacancy formation energies at tungsten grain boundaries from local structure via machine learning method, J. Nucl. Mater. 559 (2022).
- [11] J. Messina, R. Luo, K. Xu, G. Lu, H. Deng, M.A. Tschopp, F. Gao, Machine learning to predict aluminum segregation to magnesium grain boundaries, Scr. Mater. 204 (2021)
- [12] K. Guo, Z. Yang, C.H. Yu, M.J. Buehler, Artificial intelligence and machine learning in design of mechanical materials, Mater. Horiz. 8 (4) (2021) 1153–1172.
- [13] C. Wen, C. Wang, Y. Zhang, S. Antonov, D. Xue, T. Lookman, Y. Su, Modeling solid solution strengthening in high entropy alloys using machine learning, Acta Mater. 212 (2021).
- [14] Z. Nie, H. Jiang, L.B. Kara, Stress field prediction in cantilevered structures using convolutional neural networks, J. Comput. Inf. Sci. Eng. 20 (1) (2020).
- [15] W. Dai, H. Wang, Q. Guan, D. Li, Y. Peng, C.N. Tomé, Studying the micromechanical behaviors of a polycrystalline metal by artificial neural networks, Acta Mater. 214 (2021).
- [16] J.R. Mianroodi, N. H. Siboni, D. Raabe, Teaching solid mechanics to artificial intelligence—a fast solver for heterogeneous materials, npj Comput. Mater. 7 (1) (2021).
- [17] W. Muhammad, A.P. Brahme, O. Ibragimova, J. Kang, K. Inal, A machine learning framework to predict local strain distribution and the evolution of plastic anisotropy & fracture in additively manufactured alloys, Int. J. Plast. 136 (2021).
- [18] R.B. Vieira, J. Lambros, Machine learning neural-network predictions for grain-boundary strain accumulation in a polycrystalline metal, Exp. Mech. 61 (4) (2021) 627–639.
- [19] Z. Yang, C.H. Yu, M.J. Buehler, Deep learning model to predict complex stress and strain fields in hierarchical composites, Sci. Adv. 7 (15) (2021).
- [20] Z. Yang, C.-H. Yu, K. Guo, M.J. Buehler, End-to-end deep learning method to predict complete strain and stress tensors for complex hierarchical composite microstructures. J. Mech. Phys. Solids 154 (2021).
- [21] Y. Cui, H.B. Chew, Machine-learning prediction of atomistic stress along grain boundaries, Acta Mater. 222 (2022).
- [22] S. Mohammadzadeh, E. Lejeune, Predicting mechanically driven full-field quantities of interest with deep learning-based metamodels, Extrem. Mech. Lett. 50 (2022) 101566.
- [23] Y.-C. Hsu, C.-H. Yu, M.J. Buehler, Tuning mechanical properties in polycrystalline solids using a deep generative framework, Adv. Eng. Mater. 23 (4) (2021).
- [24] A.J. Lew, C.-H. Yu, Y.-C. Hsu, M.J. Buehler, Deep learning model to predict fracture mechanisms of graphene, npj 2D Mater. Appl. 5 (1) (2021).
 [25] Y. Wang, D. Oyen, W. Guo, A. Mehta, C.B. Scott, N. Panda, M.G. Fernández-Godino,
- G. Srinivasan, X. Yue, StressNet deep learning to predict stress with fracture propagation in brittle materials, npj Mater. Degrad. 5 (1) (2021).
- [26] M.S.R. Elapolu, M.I.R. Shishir, A. Tabarraei, A novel approach for studying crack propagation in polycrystalline graphene using machine learning algorithms, Comput. Mater. Sci. 201 (2022).
- [27] M. Mirza, S. Osindero, Conditional generative adversarial nets, arXiv:1411.1784, arXiv Prepr. (2014). arXiv:1411.1784.
- [28] M.C. Marinica, L. Ventelon, M.R. Gilbert, L. Proville, S.L. Dudarev, J. Marian, G. Bencteux, F. Willaime, Interatomic potentials for modelling radiation defects and dislocations in tungsten, J. Phys. Condens. Matter 25 (39) (2013) 395502.
- [29] P. Hirel, Atomsk: A tool for manipulating and converting atomic data files, Comput. Phys. Commun. 197 (2015) 212–219.
- [30] A.P. Thompson, H.M. Aktulga, R. Berger, D.S. Bolintineanu, W.M. Brown, P. S. Crozier, P.J. in 't Veld, A. Kohlmeyer, S.G. Moore, T.D. Nguyen, R. Shan, M. J. Stevens, J. Tranchida, C. Trott, S.J. Plimpton, LAMMPS a flexible simulation tool for particle-based materials modeling at the atomic, meso, and continuum scales, Comput. Phys. Commun. 271 (2022) 108171.
- [31] P. Isola, J.-Y. Zhu, T. Zhou, A.A. Efros, Image-to-image translation with conditional adversarial networks, Proc. IEEE Conf. Comput. Vis. Pattern Recognit. (2017) 1125–1134
- [32] D.J. Ji, J. Park, D.-H. Cho, ConvAE: a new channel autoencoder based on convolutional layers and residual connections, IEEE Commun. Lett. 23 (10) (2019) 1769–1772.
- [33] I.E. Abdou, W.K.J.Potl. Pratt, Quantitative design and evaluation of enhancement/ thresholding edge detectors, 67(5) (1979) 753-763.
- [34] M. Li, D. Chen, S. Liu, F. Liu, Grain boundary detection and second phase segmentation based on multi-task learning and generative adversarial network, Measurement 162 (2020).
- [35] C. Lopez-Molina, B. De Baets, H. Bustince, Quantitative error measures for edge detection, Pattern Recognit. 46 (4) (2013) 1125–1139.